Journal of Applied Physics

Temperature dependence of three-dimensional domain wall arrangement in ferroelectric $K_{0.9}Na_{0.1}NbO_3$ epitaxial thin films

Cite as: J. Appl. Phys. **128**, 184101 (2020); https://doi.org/10.1063/5.0029167
Submitted: 10 September 2020 . Accepted: 25 October 2020 . Published Online: 09 November 2020

Martin Schmidbauer, Laura Bogula, Bo Wang, Michael Hanke, Leonard von Helden, Adriana Ladera, Jian-Jun Wang, Long-Qing Chen, and Jutta Schwarzkopf

AIP Publishing

Journal of Applied Physics ARTICLE scitation.org/journal/jap

Temperature dependence of three-dimensional domain wall arrangement in ferroelectric $K_{0.9}Na_{0.1}NbO_3$ epitaxial thin films

Cite as: J. Appl. Phys. **128**, 184101 (2020); doi: 10.1063/5.0029167
Submitted: 10 September 2020 · Accepted: 25 October 2020 ·
Published Online: 9 November 2020

Martin Schmidbauer,[1,a)] Laura Bogula,[1] Bo Wang,[2] Michael Hanke,[3] Leonard von Helden,[1] Adriana Ladera,[2,4] Jian-Jun Wang,[2] Long-Qing Chen,[2] and Jutta Schwarzkopf[1]

AFFILIATIONS

[1] Leibniz-Institut für Kristallzüchtung, Max-Born-Str. 2, 12489 Berlin, Germany
[2] Materials Research Institute and Department of Materials Science and Engineering, The Pennsylvania State University, University Park, Pennsylvania 16802, USA
[3] Paul-Drude-Institut für Festkörperelektronik, Hausvogteiplatz 5-7, 10117 Berlin, Germany
[4] Department of Computer Science and Engineering, University of South Florida, Tampa, Florida 33620, USA

Note: This paper is part of the Special Topic on Domains and Domain Walls in Ferroic Materials

[a)] **Author to whom correspondence should be addressed:** martin.schmidbauer@ikz-berlin.de

ABSTRACT

The three-dimensional arrangement and orientation of domain walls in ferroelectric $K_{0.9}Na_{0.1}NbO_3$/(110)$NdScO_3$ epitaxial thin films were investigated at different temperatures both experimentally by means of piezoresponse force microscopy and three-dimensional x-ray diffraction and theoretically by three-dimensional phase-field simulations. At room temperature, a well-ordered herringbone-like domain pattern appears in which there is a periodic arrangement of a_1a_2/M_C monoclinic phases. Four different types of domain walls are observed, which can be characterized by out-of-plane tilt angles of ±45° and in-plane twist angles of ±21°. For the orthorhombic high-temperature phase, a periodic a_1/a_2 stripe domain pattern with exclusive in-plane polarization is formed. Here, two different types of domain walls are observed, both of them having a fixed out-of-plane domain wall angle of 90° but distinguished by different in-plane twist angles of ±45°. The experimental results are fully consistent with three-dimensional phase-field simulations using anisotropic misfit strains. The qualitative agreement between the experiment and the theory applies, in particular, to the wide phase transition range between about 180 °C and 260 °C. In this temperature range, a complex interplay of coexisting monoclinic a_1a_2/M_C and orthorhombic a_1/a_2 phases takes place.

I. INTRODUCTION

Domains play a central role in ferroic materials.[1,2] Their formation is driven by the total free energy, which is—for ferroelectrics—mainly determined by the chemical, electrostatic, elastic, and domain wall energies. Ferroelectric domain walls are especially interesting since they often exhibit different electrical and structural characteristics than the surrounding materials.[3] Their orientations are determined by the mechanical and electrostatic compatibility conditions at the interface. The properties of domain walls are particularly important, since they can be generated, moved, and transformed by an external electric field,[4,5] which has a significant impact on the feasibility of domain wall nanoelectronics. In thin films, the volume fraction of ferroelectric domain walls is often increased compared to bulk crystals in order to relax strain energy due to substrate constraints,[6] potentially providing a large influence on the ferro- and piezoelectric properties of the films. Therefore, detailed knowledge of the relationship between morphological/structural and piezo-/ferroelectric properties of domains and domain walls is especially important for thin films.

In many ferroelectric materials, the electrical polarization vector and possible domain walls are linked to fixed main crystallographic directions. For example, in ferroelectrics with a tetragonal symmetry, the corresponding walls separating domains with different polarization vectors can only be tilted relative to the main crystallographic axes by angles of 45°, 90°, or 180°.[7,8] In contrast, in ferroelectric systems with a monoclinic crystal symmetry, domain walls can exist in low-symmetric orientations with high Miller indices. In a theoretical work, Bokov and Ye[9] were able to show that the domain wall angles depend essentially on the geometry and dimension of the monoclinic unit cell, in particular, on the monoclinic angle and the lattice parameters. Monoclinic ferroelectric thin films are, therefore, of high fundamental and technological interest, as they combine a flexible domain wall arrangement[10] with improved ferro-/piezoelectric properties.[11–13]

In this respect, the solid solution $K_xNa_{1-x}NbO_3$[14,15] is an intriguing material, because it is lead-free and exhibits excellent ferro-/piezoelectric properties. The existence of monoclinic phases has been predicted in the framework of the Landau–Ginzburg theory[16–18] and experimentally confirmed.[19–21] However, these theoretical investigations are limited to the treatment of single-domain or preset simple polydomain systems.[22,23] Recently, Wang *et al.* have performed phase-field simulations to obtain the equilibrium domain structures and establish the temperature-misfit strain phase diagram considering phase coexistence,[24] although anisotropic mismatch strains are not yet included in these calculations.

Lattice strains determine not only the phase symmetry and domain wall arrangement in epitaxial films but also have a crucial influence on phase transitions. In a previous paper,[25] we have revealed that $K_{0.9}Na_{0.1}NbO_3$ thin films on $NdScO_3$ (NSO) substrates undergo a ferroelectric-to-ferroelectric phase transition at high temperatures. The phase transition transforms a complex herringbone-like domain pattern with an alternating monoclinic a_1a_2/M_C domain arrangement[26] to an orthorhombic phase, which appears as a very regular a_1/a_2 stripe domain pattern that occurs in four different variants of superdomains. However, the three-dimensional (3D) arrangement and orientation of the domain walls are still largely unexplored for both the room temperature and high-temperature phase.

Therefore, in this paper, we have carried out 3D x-ray diffraction, which is sensitive to the 3D arrangement and orientation of domain walls and provides additional information about the structural properties of the involved ferroelectric phases and domain walls. In parallel, we have performed 3D phase-field simulations, which are a powerful tool as they combine thermodynamics and kinetics to simulate the formation and evolution of ferroelectric domains on a mesoscopic length scale. Within this work, we take a closer look at the 3D domain wall arrangement and find very good agreement between simulations and experimental data. This is especially valid for the wide phase transition regime within which coexistence between the a_1a_2/Mc room temperature phase and the a_1/a_2 high-temperature phase is observed. The excellent agreement between the experiment and simulation opens up interesting perspectives with respect to intentional domain engineering in strained ferroelectric thin films.

The present work is structured as follows. In Sec. II, we first give a short introduction to the 3D phase-field model for ferroelectric thin films, followed by an experimental Sec. III, in which we briefly present the method of fast 3D x-ray diffraction and its practical implementation at a highly brilliant synchrotron radiation source. In Sec. IV, our experimental and theoretical results are presented and discussed.

II. THEORY

The phase-field method has been established as a powerful approach to model complex domain structures at equilibrium and to calculate their evolution under external stimuli for ferroelectric bulk crystals and epitaxial thin films.[27,28] The ferroelectric system is modeled by taking the spontaneous polarization $\boldsymbol{P}(\boldsymbol{r}, t)$ as the order parameter. The evolution of the order parameter is described by the time-dependent Ginzburg–Landau (TDGL) equation,

$$\frac{\partial \boldsymbol{P}}{\partial t} = -L\frac{\delta F}{\delta \boldsymbol{P}}, \tag{1}$$

where F is the total free energy of the system and L is the kinetic coefficient. Several energy contributions including the Landau energy, elastic energy, electrical energy, and gradient energy are considered here, i.e.,

$$F = \int_V (f_{Landau} + f_{elastic} + f_{electric} + f_{gradient})dV. \tag{2}$$

The detailed formulation of each individual term is described in Ref. 27. The TDGL equation is solved iteratively to obtain the polarization distribution at equilibrium by adopting the semi-implicit Fourier transformation method, which is implemented in the phase-field package μ-Pro®. At each time step, we solve the elastostatic equation subject to the mixed-type mechanical boundary condition for epitaxial thin films and the electrostatic equation under the short-circuit electrical boundary condition at the top and bottom surfaces.[29,30] Two-dimensional periodical boundary conditions are used for all equations in the in-plane directions of the system. A detailed formulation of the phase-field model for ferroelectric thin films is given in Refs. 27 and 28. All Landau parameters, elastic stiffness, and electrostrictive coefficients are adopted from previous Landau–Devonshire models of single-crystalline $K_xNa_{1-x}NbO_3$.[31,32]

Here, we performed three-dimensional phase-field simulations to obtain the equilibrium domain structures of $K_{0.9}Na_{0.1}NbO_3$ epitaxial thin films at room temperature and to examine the domain evolution during phase transition at elevated temperatures. We choose an orthogonal coordinate system (x, y, z) in which x is parallel to the $[001]_{NSO}$ direction, y is parallel to the $[\bar{1}10]_{NSO}$ direction, and z is parallel to the surface normal of the (110) oriented $NdScO_3$ (NSO) orthorhombic substrate. The 3D system is discretized into $256\Delta x \times 256\Delta y \times 60\Delta z$ grid points, where $\Delta x = \Delta y = \Delta z = 1$ nm. The film thickness is taken as 35 nm, while a 20 nm-thick region for the nonpolar substrate is utilized to impose the zero displacement boundary condition at the bottom of the system. The remaining 5 nm-thick layers are taken as air. To obtain the equilibrium domain structure for the ferroelectric thin film at room temperature, the system is evolved from a small random noise of polarization for sufficiently long time to relax.

According to the strain-temperature phase diagram of $K_xNa_{1-x}NbO_3$ thin films, there is a phase coexistence region near room temperature under low misfit strains, where the domain structures are complex.[28] Therefore, to obtain the coexistence of multiple domain variants with a regular pattern, a simple a_1a_2/M_C

polydomain structure is preset to serve as a precursor along with the random noise. For $K_{0.9}Na_{0.1}NbO_3$ on orthorhombic (110) $NdScO_3$, the misfit strain is strongly anisotropic with respect to the cubic paraelectric reference state with compressive strain $\varepsilon_{xx} = -0.16\%$ along $[001]_{NSO}$ and tensile strain $\varepsilon_{yy} = 0.15\%$ along $[\bar{1}10]_{NSO}$. These strain conditions are located at the phase boundary between the stability regions for M_{C1}/M_{C2} and a_1a_2/M_C in the calculated misfit strain–misfit strain diagram[33] leading to instabilities in the simulation. However, it is known from experiments that a herringbone-like domain arrangement can be stabilized even for slightly different strain conditions.[10] Furthermore, it must be considered that the elastic stiffness and electrostriction coefficients are not exactly known for $K_{0.9}Na_{0.1}NbO_3$, which can lead to additional uncertainties in the determination of phase boundaries.

Therefore, we have selected a strain condition for the theoretical simulations, which results likewise in a herringbone-like domain pattern but is much more stable to slight parameter variations. Specifically, we assume a relatively large anisotropic misfit strain of $\varepsilon_{xx} = 0.0\%$ and $\varepsilon_{yy} = 1.0\%$ in the simulations. Also, note that the misfit strains are assumed to be constant in the investigated temperature range due to the similar thermal expansion coefficients for $NdScO_3$[34] and $KNbO_3$.[35] In this paper, we will show that our specific selection of mismatch strains leads to a very good agreement between the simulation and the experiment. This means that even though the experimental and simulated conditions are not fully comparable, our phase-field simulations provide a reasonable solution in this system considering the energy terms given in Eq. (2). However, we would like to stress that the agreement between the simulation and the experiment is only qualitative, while quantities such as the lateral dimensions of domains or the phase transition temperature cannot be compared on a quantitative scale.

III. EXPERIMENTAL METHODS

$K_{0.9}Na_{0.1}NbO_3$ thin films were epitaxially grown on (110) $NdScO_3$ orthorhombic substrates by liquid-delivery spin metal-organic vapor phase epitaxy (MOVPE). In comparison to physical growth techniques such as pulsed laser deposition[36,37] or magnetron sputtering,[38] epitaxial growth takes place close to the thermodynamic equilibrium and at relatively high oxygen partial pressures of typically 10–20 mbar. This leads to nearly perfect thin films with smooth surfaces/interfaces and very regular ferroelectric domain patterns. In this work, we present results obtained on samples with 38 and 52 nm film thickness. These films are very similar in their domain pattern. Further details on the samples and growth parameters are given in Refs. 21 and 39.

Using piezoresponse force microscopy (PFM), ferroelectric domains can be imaged with nanometer resolution, and corresponding statements about the three-dimensional orientation of the electrical polarization vector can be made. However, PFM images do not provide depth resolution so that the three-dimensional information about the spatial arrangement and orientation of domain walls is not accessible. On the other hand, high-resolution x-ray diffraction (HRXRD) is an effective method that is sensitive to (i) the orientation of domain walls, (ii) their periodic arrangement, and, additionally, (iii) lattice strains. A critical comparison of HRXRD and PFM is particularly advantageous because it allows ferro-/piezoelectric properties to be correlated with corresponding structural features. Each of these structural properties listed above is three-dimensional in nature, and we will demonstrate in this paper that HRXRD allows the independent study of each feature.

The x-ray diffraction patterns of crystalline materials contain crystal truncation rods (CTRs) when surfaces or interfaces are present.[40,41] Similarly, domain walls also induce a rod-shaped intensity distribution in reciprocal space, which is directed along the domain wall normal. If the domain walls are periodically arranged, the intensity within the CTRs is periodically modulated, and sharp satellite reflections arise. Their periodicity in reciprocal space inversely scales with the periodicity in real space. Finally, lattice strains (e.g., shearing and local rotation of unit cells within adjacent domains) often lead to peak splitting, which is the characteristic for the ferroelectric phase present.[26] In summary, due to the three-dimensional nature of lattice strains and domain (wall) arrangement, only 3D reciprocal space maps of diffracted intensity give access to the full information. Rapid 3D measurements are feasible, but they require the use of intense synchrotron radiation in combination with high-frame rate two-dimensional detectors.[42,43]

The x-ray measurements were performed at the synchrotron radiation facility PETRA III (DESY, Hamburg) at the experimental station P08 using an x-ray energy of 15 keV. A two-dimensional detector (DECTRIS PILATUS) with a pixel size of $172\,\mu$m was placed at a distance of 940 mm from the sample. To achieve a good angular resolution in both vertical and horizontal directions, primary apertures of typically $150 \times 150\,\mu\text{m}^2$ were used. A three-dimensional image of the scattered intensity distribution can then be obtained very quickly by a simple rocking scan of the sample. Depending on the desired angular resolution and counting statistics, typical measurement times vary between several minutes and a few hours.

In order to be sensitive to the domain walls of both the a_1a_2/M_C room temperature structure and the a_1/a_2 high-temperature structure, we have chosen the $(620)_{NSO}$ asymmetrical Bragg reflection. For both phases, the $(620)_{NSO}$ reflection gives suitable information about the domain wall arrangement and orientation. Moreover, it is particularly well-suited because the atomic lattice of the epitaxial layer is not distorted along the in-plane $[\bar{1}10]_{NSO}$ substrate direction.[44] Thus, the orientation and intensity modulation of the CTRs in reciprocal space can be used to directly determine the orientation and the spatial arrangement of the 3D domain walls.

During the x-ray investigations, an Anton Paar DHS 1100 temperature chamber[45] was used to heat the samples. To ensure good thermal contact of the samples, they were glued to a copper sample holder, which was mounted directly on the heating plate. Piezoresponse force microscopy (Asylum Research, MFP-3D standalone) was applied in the dual AC resonance tracking mode.

IV. RESULTS AND DISCUSSION

A. Room temperature

The room temperature phase of anisotropically strained $K_{0.9}Na_{0.1}NbO_3$/(110) $NdScO_3$ thin films shows a characteristic herringbone-like domain arrangement as displayed in the piezoresponse force image in Fig. 1(a). This domain pattern is formed by a

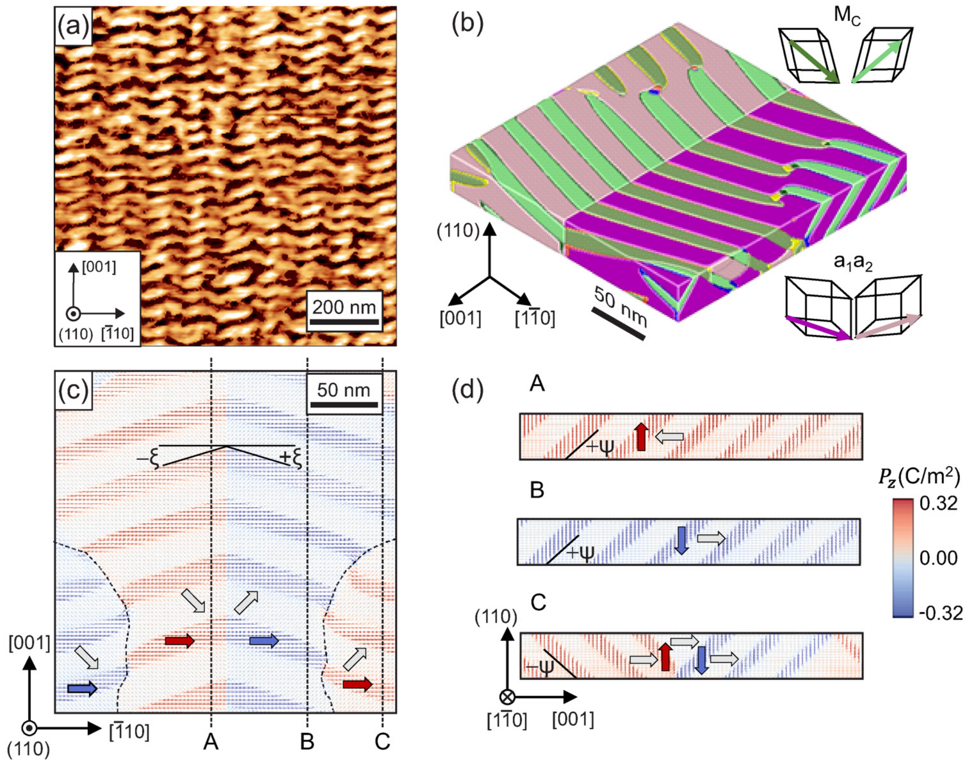

FIG. 1. Herringbone-like a_1a_2/M_C domain structure at room temperature. (a) Lateral piezoresponse force micrograph ($1 \times 1\,\mu m^2$) of a 38 nm $K_{0.9}Na_{0.1}NbO_3$ thin film grown on (110) $NdScO_3$. (b) Phase-field simulation ($256 \times 256\,nm^2$) of the 3D domain structure calculated for $\varepsilon_{xx} = 0.0\%$ and $\varepsilon_{yy} = 1.0\%$ together with the unit cells and polarization vectors of the M_C and a_1a_2 domains. (c) Corresponding simulated 2D mappings of electrical polarization vectors at the film surface. The dashed lines A, B, and C indicate the positions of respective section cuts. The twist angle ξ of the herringbone-like pattern is labeled. (d) 2D maps of polarization vectors at three sections of the x–z plane corresponding to the positions A, B, and C denoted in (c). The angle ψ of the inclined domain wall viewed from [1$\bar{1}$0] is labeled. The arrows show the overall polarization direction of each domain for better visualization. The orthogonal coordinate system refers to the orthorhombic $NdScO_3$ substrate.

coexistence of monoclinic a_1a_2 and M_C phases.[26] Their respective unit cells are depicted in Fig. 1(b), with the colored arrows indicating the electrical polarization vector of each monoclinic unit cell. For the in-plane a_1a_2 ferroelectric phase, the unit cells exhibit alternating in-plane monoclinic distortion angles and pure in-plane polarization. On the other hand, for the inclined M_C phase, the monoclinic distortion shows up in a vertical plane of the pseudocubic unit cell, leading to an inclined polarization vector, with the in-plane component along $[\bar{1}10]_{NSO}$. More detailed information about the monoclinic phases at room temperature can be found in literature, e.g., Ref. 26.

From Fig. 1(a), we can state that the a_1a_2/M_C domains are periodically arranged along the $[001]_{NSO}$ direction. The domain walls separating the two phases are smooth but are alternately inclined by about $\xi_{PFM} = \pm 20°$ relative to the $[\bar{1}10]_{NSO}$ direction. The same ordering of the a_1a_2/M_C domains in a herringbone-like domain arrangement was also obtained by phase-field calculations under the anisotropic misfit strains, as shown in Fig. 1(b). Two possible a_1a_2 and two possible M_C polar domain variants appear in the calculated domain pattern. Thus, four superdomain variants of a_1a_2/M_C can form, i.e., pink/dark green, pink/light green, violet/dark green, and violet/light green. The domain walls separating the a_1a_2/M_C phases are inclined by $\psi = \pm 45°$ with respect to the sample surface (looking from the $[1\bar{1}0]_{NSO}$ direction) and are—depending on the superdomain type—twisted by the herringbone angle, which is measured to be around $\xi = \pm 19°$ and compares reasonably well with the PFM image in Fig. 1(a).

To examine the polarization direction of each domain, we map the distributions of polarization vectors at the film surface in Fig. 1(c) along with three sections in Fig. 1(d) cut along the $[001]_{NSO}$ direction at positions labeled by A, B, and C in Fig. 1(c). It is shown that the in-plane polarization component within the M_C domains are all along the $[\bar{1}10]_{NSO}$ direction, where a tensile misfit strain is imposed on the film. At the junctions of two types of superdomains, the polarization vectors arrange in a head-to-tail configuration and form the flux-closure pattern [as seen in section C in Fig. 1(d)] to minimize the electrostatic energy. It is found that the boundaries between the superdomains can be straight (along $[001]_{NSO}$) or meandering as denoted by the thin dashed curves in Fig. 1(c). A straight boundary appears when the inclination angles ψ of the adjacent superdomains 1 and 2 are identical (e.g., $\psi_1 = \psi_2 = +45°$), as is the case in sections A and B, while it becomes curved when the angles ψ are not matching ($\psi_1 = +45° \neq \psi_2 = -45°$), such as that between sections B and C. This curving of the superdomain boundary is likely due to the relaxation of elastic energy associated with the mechanically incompatible domain walls.

Since PFM images provide only the in-plane arrangement of the ferroelectric domain walls, three-dimensional x-ray diffraction (3D-HRXRD) has been performed for in-depth information of the domain walls. Figure 2(a) exemplarily shows the 3D intensity distribution of the 52 nm thin film in the vicinity of the $(620)_{NSO}$ reciprocal lattice point (Multimedia view). The scattered signal from the $K_{0.9}Na_{0.1}NbO_3$ thin film is located at smaller Q_{110} values relative to

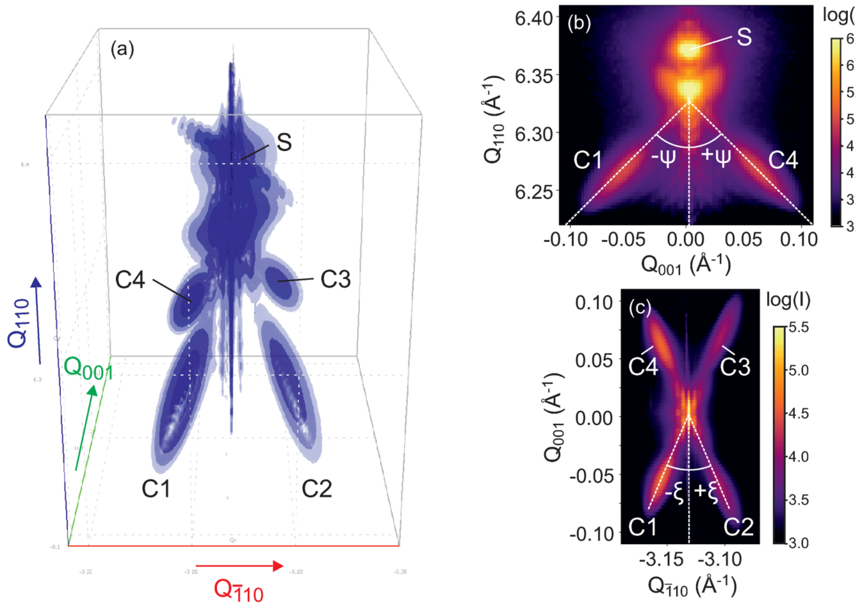

FIG. 2. (a) 3D-HRXRD intensity distribution of a 52 nm $K_{0.9}Na_{0.1}NbO_3$ thin film in the vicinity of the $(620)_{NSO}$ substrate Bragg reflection (marked as "S") recorded at 30 °C. Selected (b) out-of-plane and (c) in-plane 2D sections with the viewing direction along (b) $Q_{1\bar{1}0}$ and (c) Q_{110}, respectively. Multimedia view: https://doi.org/10.1063/5.0029167.1

the sharp substrate Bragg reflection (marked as "S"), and it is extended in reciprocal space. In particular, four prominent, differently oriented CTRs can be clearly distinguished, which are designated as C1–C4 in Fig. 1(a). They are attributed to the four types of internal domain walls seen in the phase-field simulation. More detailed information can be extracted from selected two-dimensional (2D) views. In these 2D sections [Figs. 2(b) and 2(c)], the in-plane ("twist") and out-of-plane ("tilt") angles of the four types of domain walls can be quantitatively evaluated. For example, the Q_{001}–Q_{110} out-of-plane section shown in Fig. 2(b) provides a tilt angle ψ relative to the sample surface of either $\psi = +45°$ or $\psi = -45°$ for all four types of domain walls. On the other hand, the in-plane twist angles ξ of the domain walls can be evaluated from the Q_{001}–Q_{-110} in-plane section as shown in Fig. 2(c). The corresponding values of $\xi = \pm 21°$ are in good agreement with the experimental ($\xi_{PFM} = 20°$) and simulated ($\xi = \pm 19°$) herringbone angles in Figs. 1(a) and 1(b), respectively.

In summary, all four different types of domain walls predicted by the phase-field simulation are also observed in the 3D-HRXRD measurements. This confirms the high-index nature of the domain walls, which are inherently different from ferroelastic domain walls of other higher symmetrical ferroelectric phases of perovskite oxides, such as the 90°-domain walls in a tetragonal phase and the 71°- and 109°-domain walls in a rhombohedral phase. Also the experimentally determined tilt angle of $\psi = \pm 45°$ is completely consistent with the simulations.

B. High temperature

When heating the thin films to higher temperatures, we observe a ferroelectric-to-ferroelectric phase transition. This can be inspected in the lateral piezoresponse force image for the 38 nm sample taken at 250 °C in Fig. 3(a). The herringbone-like domain arrangement present at room temperature [Fig. 1(a)] has changed into a periodic and very regular stripe domain pattern. Two types of superdomains can be identified, which manifest themselves as light and dark areas. The light superdomains exhibit a periodic array of narrow stripe domains, where the domain walls are rotated by about $\xi = -45°$ from the $[\bar{1}10]_{NSO}$ direction. Within the dark superdomains, no internal contrast is detected. However, for reasons of symmetry and x-ray measurements discussed below, we expect a similar stripe domain pattern with domain walls rotated by $\xi = +45°$. In a recently published paper,[25] we have shown that the stripe domain pattern consists of slightly rotated orthorhombic unit cells, finally leading to an a_1/a_2 domain arrangement with exclusive horizontal electrical polarization. For more detailed information about the unit cell symmetry and structural properties of the high-temperature phase, we refer the reader to Ref. 25.

The stripe domain pattern has also been obtained in phase-field simulations by raising the temperature up to 327 °C from the herringbone-like domains at room temperature [Fig. 1(c)]. Here, we first show the equilibrium high-temperature domain structure in Fig. 3(b), while the phase transition and domain evolution during the heating process are left for Sec. IV C. The simulated high-temperature domain pattern consists of two stripe-like superdomains, i.e., the orange/black and champagne/black twin polydomains in Fig. 3(b). For each domain variant, the polarization vector lies within the surface plane with alignment either along $[001]_{NSO}$ (a_1 domains) or along $[\bar{1}10]_{NSO}$ (a_2 domains). The domain walls between the a_1/a_2 stripes are perpendicular to the surface plane, with in-plane twist angles of $\xi = \pm 45°$. The width of the a_2 domain is significantly larger than that of a_1 domains because of the assumed larger anisotropic misfit strain. Specifically, the tensile misfit strain along $[\bar{1}10]_{NSO}$ ($\varepsilon_{yy} = 1.0\%$) strongly favors the polar axis of the unit cell to be aligned toward the y axis for lower elastic

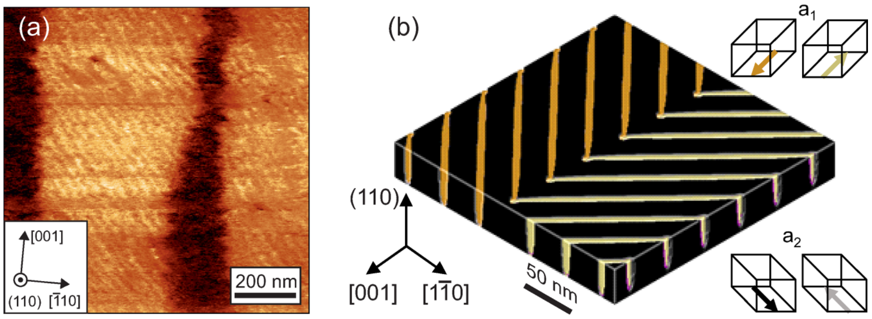

FIG. 3. (a) Lateral piezoresponse force micrograph (1 × 1 μm^2) of a 38 nm $K_{0.9}Na_{0.1}NbO_3$ thin film grown on (110) $NdScO_3$ substrate taken at 250 °C. (b) Phase-field simulation (256 × 256 nm^2) of the 3D domain structure calculated for 327 °C. The unit cells of a_1 and a_2 domains are shown on the right-hand side together with the respective electrical polarization vectors. The orthogonal coordinate system refers to the orthorhombic $NdScO_3$ substrate.

strain energy. We also notice that the high-temperature stripe-like domain pattern inherits to some extent the room-temperature herringbone pattern. This similarity is illustrated by the fact that the straight superdomain boundary along $[001]_{NSO}$ found in the herringbone-like pattern is also maintained in the high-temperature domain pattern, which is again consistent with the PFM images in Figs. 1(a) and 3(a).

The corresponding 3D-HRXRD intensity distribution is shown in Fig. 4(a) (Multimedia view). Compared to room temperature [Fig. 2(a)], drastic differences can be observed. In particular, the four strong and inclined CTRs (C1–C4) have disappeared. Instead, a complicated and very rich diffraction pattern has formed. On the one hand, strong vertically aligned CTRs can be observed, which are caused by the sample surface and the film/substrate interface. They exhibit pronounced vertical intensity fringes caused by the finite thickness of the thin film, as can be examined in detail in a selected out-of-plane 2D section in Fig. 4(b). Furthermore, in an in-plane 2D section [Fig. 4(c)], we also observe four strong horizontally aligned CTRs, each at 90° to each other. They also show strong intensity fringes (satellite peaks), which indicate well-ordered domain walls oriented perpendicular to the sample surface. From these 2D sections, in-plane domain wall twist angles of $\xi = \pm 45°$ and out-of-plane domain wall tilt angles of $\psi = 90°$ can be evaluated.

The x-ray diffraction data again fit very well to the corresponding phase-field simulations. This concerns mainly the observation of two different types of domain walls and the agreement of the corresponding out-of-plane tilt angles ($\psi = 90°$) and in-plane twist angles ($\xi = \pm 45°$) in both the simulation and the experiment.

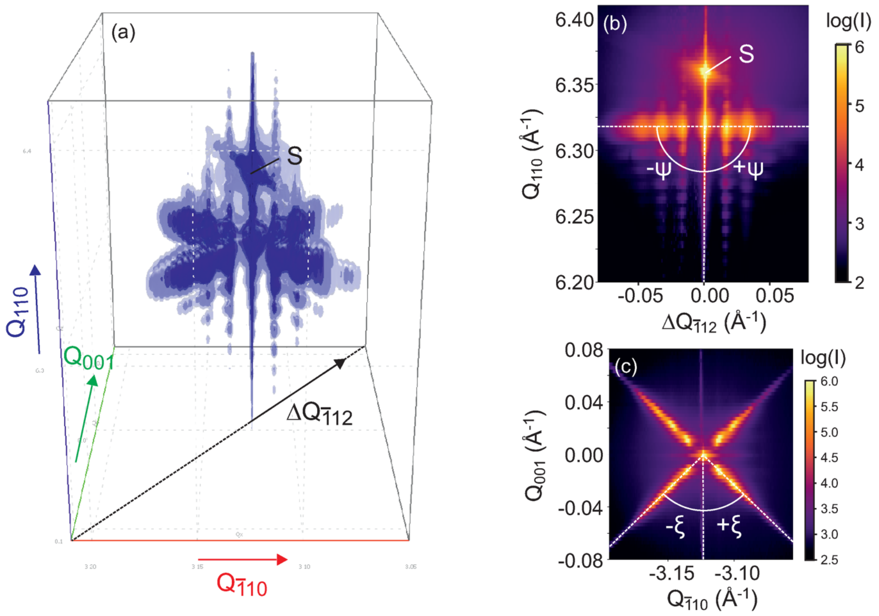

FIG. 4. (a) 3D-HRXRD intensity distribution of a 52 nm film in the vicinity of the $(620)_{NSO}$ substrate Bragg reflection (marked as “S”) recorded at 260 °C. Selected (b) out-of-plane ($\Delta Q_{\bar{1}12} - Q_{110}$) and (c) in-plane ($Q_{\bar{1}10} - Q_{001}$) 2D sections. Multimedia view: https://doi.org/10.1063/5.0029167.2

C. Coexistence regime

Having discussed the room temperature ferroelectric phase and the high-temperature ferroelectric phase separately in the previous chapters, we now want to focus our attention on the extended temperature range within which the phase transition takes place and in which we have experimentally observed a coexistence regime between different ferroelectric phases.[25]

For this reason, phase-field simulations were performed using a preset herringbone domain arrangement at equilibrium at room temperature, see Fig. 5(a) [replotted the same figure here as in Fig. 1(b)]. The domain evolution at elevated temperatures is captured by incrementally raising the temperature and relaxing the system (by 25 K every 10 000 time steps). For simplicity, we assume that the misfit strain does not change with temperature. As the system is heated up to 177 °C, two superdomain variants that have different inclination angles in their domain walls [regions with curved boundaries, as seen in Fig. 1(c) section C] disappear first [Fig. 5(b)]. Continuing to raise the temperature leads to the vanishing of the entire herringbone pattern as the M_C phase disappears, and only the a_1a_2 phase remains [Fig. 5(c)]. With the disappearance of the herringbone pattern, the inner domain walls with $\psi = \pm 45°$ inclination angle are no longer existent. When further increasing the temperature to 277 °C [Fig. 5(d)], the orthorhombic high-temperature phase has additionally formed, which manifests itself in an a_1/a_2 stripe domain pattern [Fig. 5(e)], preferably starting from the sample surface. We also observe a coexistence between the monoclinic a_1a_2 phase at the film/substrate interface and the orthorhombic a_1/a_2 phase at the film surface at 302 °C. This coexistence disappears when proceeding further to 327 °C [Fig. 5(f)], where only the orthorhombic a_1/a_2 phase remains.

In order to experimentally verify the results obtained from the phase-field simulations, we have performed x-ray diffraction in the immediate proximity of the phase transition. In Fig. 6, we compare 2D in-plane intensity distributions measured at different temperatures in the vicinity of the $(620)_{NSO}$ substrate Bragg reflection. Figure 6(a) again shows the diffraction pattern obtained at 30 °C. It exhibits the four different CTRs (C1–C4) representing the four different types of domain walls typically observed in a herringbone pattern. When increasing the temperatures, the CTRs become continuously weaker [Figs. 6(b) and 6(c)], and at 180 °C [Fig. 6(d)], we observe a complete disappearance. Between 160 °C and 220 °C [Figs. 6(c)–6(f)], we can already see the typical cross-shaped intensity pattern characteristic for the orthorhombic a_1/a_2 stripe domains, even though it is still rather weak. With further temperature increase to 240 °C [Fig. 6(g)] and 260 °C [Fig. 6(h)], the in-plane satellite peaks fully emerge, indicating that the phase transition to the orthorhombic phase is completed.

It turns out that the experimental temperature values do not exactly match those in the simulations. This may be due to the fact that the misfit strain for stabilizing the herringbone structure is different in the simulations and the assumption that this misfit strain remains unchanged upon heating. Nevertheless, the experimental data shown in Fig. 6 agree qualitatively well with the corresponding phase-field simulations shown in Fig. 5. However, please note that the $(620)_{NSO}$ Bragg reflection is not sensitive to the monoclinic a_1a_2 phase, because it does not exhibit the corresponding characteristic in-plane peak splitting. Therefore, based on Fig. 6, we cannot directly confirm a gradual transformation of the M_C phase into the a_1a_2 phase as predicted by the simulations. This also concerns the predicted coexistence of a_1a_2 and a_1/a_2 phases at high temperatures. However, in our recently published study,[25] grazing incidence in-plane x-ray diffraction revealed that heating up to 180 °C leads to a complete disappearance of the M_C phase, while the a_1a_2 phase can always be observed. In addition, the monoclinic a_1a_2 and the orthorhombic a_1/a_2 phases coexist between about 200 °C and 220 °C. With further heating to

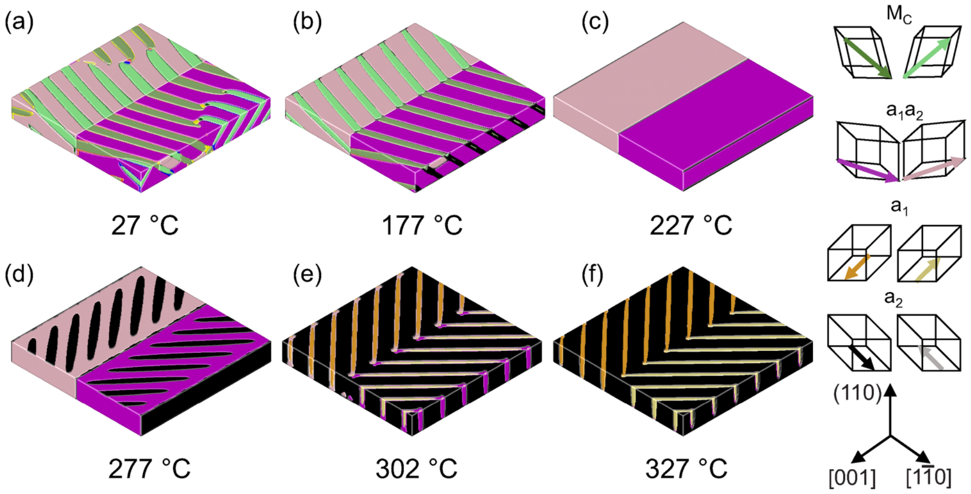

FIG. 5. Three-dimensional phase-field simulations (256 × 256 nm^2) of the phase transition and domain evolution at elevated temperatures. The corresponding unit cells together with their respective electrical polarization vectors are shown on the right-hand side. The orthogonal coordinate system refers to the orthorhombic $NdScO_3$ substrate.

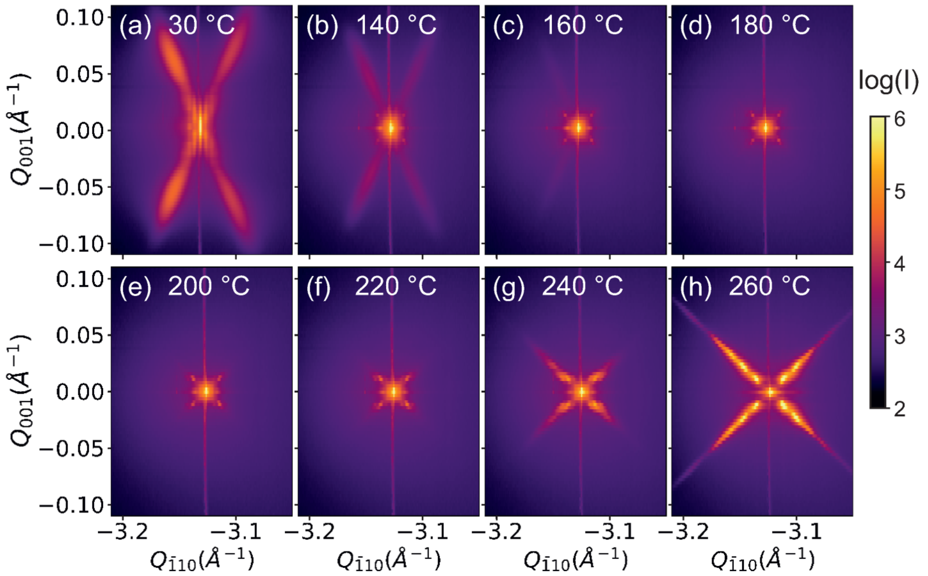

FIG. 6. In-plane two-dimensional sections for the 52 nm sample in the vicinity of the $(620)_{NSO}$ Bragg reflection as a function of temperature. The intensity was integrated along Q_{110} within the interval from 6.24 $Å^{-1}$ to 6.33 $Å^{-1}$ in order to include both room and high-temperature film features. The elongated vertical thin lines are experimental artifacts.

260 °C, the a_1a_2 phase slowly vanishes, and only the orthorhombic a_1/a_2 phase remains. This finding, together with the behavior observed in Fig. 6, finally results in an excellent agreement with the scenario predicted by the phase-field simulations in Fig. 5.

V. CONCLUSIONS

In the present work, we have investigated the three-dimensional orientation and arrangement of domain walls in $K_{0.9}Na_{0.1}NbO_3$/(110)$NdScO_3$ strained ferroelectric thin films at different temperatures. We carried out piezoresponse force microscopy and 3D x-ray diffraction patterns. In parallel, we performed 3D phase-field simulations, which take into account the anisotropic misfit strains of the epitaxial thin films. Experimental and simulated results are fully consistent for both room temperature a_1a_2/M_C and high-temperature a_1/a_2 ferroelectric phases. Particularly noteworthy is the excellent qualitative agreement in the broad phase transition regime within which the coexistence between monoclinic and orthorhombic phases is observed.

The comprehensive deployment of advanced experiment and simulation techniques allows us to understand the 3D structural configuration of complex domain structures and lower-symmetric phases in ferroelectric thin films. This routine can be generalized to other ferroelectric systems such as (111)-oriented epitaxial thin films[46] and other lead-free piezoelectrics.[47] On the other hand, it will be interesting to further investigate the domain switching behaviors in $K_{0.9}Na_{0.1}NbO_3$ thin films and engineer the 3D domain structure in order to optimize functional properties such as piezoelectricity and domain wall conductivity. However, these tasks would go beyond the scope of the present work and are intended for future investigations.

ACKNOWLEDGMENTS

We would like to thank DESY Hamburg for providing beam time at the stations P08 (Proposal No. I-20180675). We are especially grateful to Florian Bertram for technical support during the x-ray diffraction experiments and to Michaela Klann for sample growth. The $NdScO_3$ substrates were grown at Leibniz-Institut für Kristallzüchtung in the group of Steffen Ganschow. B.W. and L.-Q.C. acknowledge support by the National Science Foundation (NSF) through Grant No. DMR-1744213. A.L. acknowledges funding from the Materials Research Science and Engineering Center (MRSEC) of the Pennsylvania State University, supported by the NSF under Grant. No. DMR-1420620. We also thank EFRE (Project No. 1.8/15) and DFG (Project No. FE 1438/2-1) for funding this project. We would like to thank Matthias Bickermann for a critical reading of the manuscript. The computer simulations were performed using the commercial software package μ-PRO (http://mupro.co/contact/) on the ICS-ACI Computing Systems at Pennsylvania State University and at the Extreme Science and Engineering Discovery Environment cluster, which used the Comet system at the UC San Diego.

DATA AVAILABILITY

The data that support the findings of this study are available from the corresponding author upon reasonable request.

REFERENCES

[1] A. K. Tagantsev, L. E. Cross, and J. Fousek, *Domains in Ferroic Crystals and Thin Films* (Springer, 2010), ISBN: 978-1-4419-1417-0.
[2] *Topological Structures in Ferroic Materials*, Springer Series in Materials Science, edited by J. Seidel (Springer, 2016), ISBN: 978-3-319-25301-5.
[3] G. Catalan, J. Seidel, R. Ramesh, and J. F. Scott, "Domain wall nanoelectronics," Rev. Mod. Phys. **84**, 119–156 (2020).
[4] L. J. McGilly, P. Yudin, L. Feigl, A. K. Tagantsev, and N. Setter, "Controlling domain wall motion in ferroelectric thin films," Nat. Nanotechnol. **10**, 145–150 (2015).

[5] L. J. McGilly, L. Feigl, T. Sluka, P. Yudin, A. K. Tagantsev, and N. Setter, "Velocity control of 180° domain walls in ferroelectric thin films by electrode modification," Nano Lett. **16**, 68–73 (2016).

[6] C. Kittel, "Theory of the structure of ferromagnetic domains in films and small particles," Phys. Rev. **70**, 965–971 (1946).

[7] A. S. Everhardt, S. Matzen, N. Domingo, G. Catalan, and B. Noheda, "Ferroelectric domain structures in low-strain $BaTiO_3$," Adv. Electron. Mater. **2**, 1500214 (2016).

[8] B. Meyer and D. Vanderbilt, "*Ab initio* study of ferroelectric domain walls in $PbTiO_3$," Phys. Rev. B **65**, 104111 (2002).

[9] A. A. Bokov and Z. G. Ye, "Domain structure in the monoclinic *Pm* phase of $Pb(Mg_{1/3}Nb_{2/3})O_3$–$PbTiO_3$ single crystals," J. Appl. Phys. **95**, 6347–6359 (2004).

[10] D. Braun, M. Schmidbauer, M. Hanke, A. Kwasniewski, and J. Schwarzkopf, "Tunable ferroelectric domain wall alignment in strained monoclinic $K_xNa_{1-x}NbO_3$ epitaxial films," Appl. Phys. Lett. **110**, 232903 (2017).

[11] Z. Chen, Z. Luo, C. Huang, Y. Qi, P. Yang, L. You, C. Hu, T. Wu, J. Wang, C. Gao, T. Sritharan, and L. Chen, "Low-symmetry monoclinic phases and polarization rotation path mediated by epitaxial strain in multiferroic $BiFeO_3$ thin films," Adv. Funct. Mater. **21**, 133–138 (2011).

[12] C. Hu, X. Meng, M.-H. Zhang, H. Tian, J. E. Daniels, P. Tan, F. Huang, L. Li, K. Wang, J.-F. Li, Q. Lu, W. Cao, and Z. Zhou, "Ultra-large electric field-induced strain in potassium sodium niobate crystals," Sci. Adv. **6**, eaay5979 (2020).

[13] J. Koruza, H. Liu, M. Höfling, M.-H. Zhang, and P. Veber, "(K,Na) NbO_3-based piezoelectric single crystals: Growth methods, properties, and applications," J. Mater. Res. **35**, 990–1016 (2020).

[14] Y. Saito, H. Takao, T. Tani, T. Nonoyama, K. Takatori, T. Homma, T. Nagaya, and M. Nakamura, "Lead-free piezoceramics," Nature **432**, 84–87 (2004).

[15] P. K. Panda and B. Sahoo, "PZT to lead free piezo ceramics: A review," Ferroelectrics **474**, 128–143 (2015).

[16] N. A. Pertsev, A. G. Zembilgotov, and A. K. Tagantsev, "Effect of mechanical boundary conditions on phase diagrams of epitaxial ferroelectric thin films," Phys. Rev. Lett. **80**, 1988–1991 (1998).

[17] G. Bai and W. Ma, "Phenomenological analysis of phase transitions in epitaxial perovskite ferroelectric thin films," Phys. B Condens. Matter **405**, 1901–1907 (2010).

[18] M.-J. Zhou, J.-J. Wang, L.-Q. Chen, and C.-W. Nan, "Strain, temperature, and electric-field effects on the phase transition and piezoelectric responses of $K_{0.5}Na_{0.5}NbO_3$ thin films," J. Appl. Phys. **123**, 154106 (2018).

[19] J. Luo, W. Sun, Z. Zhou, H.-Y. Lee, K. Wang, F. Zhu, Y. Bai, Z. J. Wang, and J.-F. Li, "Monoclinic (K,Na)NbO_3 ferroelectric phase in epitaxial films," Adv. Electron. Mater. **3**, 1700226 (2017).

[20] J. Luo, W. Sun, Z. Zhou, Y. Bai, Z. J. Wang, G. Tian, D. Chen, X. Gao, F. Zhu, and J.-F. Li, "Domain evolution and piezoelectric response across thermotropic phase boundary in (K,Na)NbO_3-based epitaxial thin films," ACS Appl. Mater. Interfaces **9**, 13315–13322 (2017).

[21] J. Schwarzkopf, D. Braun, M. Hanke, R. Uecker, and M. Schmidbauer, "Strain engineering of ferroelectric domains in $K_xNa_{1-x}NbO_3$ epitaxial layers," Front. Mater. **4**, 26 (2017).

[22] V. G. Koukhar, N. A. Pertsev, and R. Waser, "Thermodynamic theory of epitaxial ferroelectric thin films with dense domain structures," Phys. Rev. B **64**, 214103 (2001).

[23] F. Xue, Y. Ji, and L.-Q. Chen, "Theory of strain phase separation and strain spinodal: Applications to ferroelastic and ferroelectric systems," Acta Mater. **133**, 147–159 (2017).

[24] B. Wang, H.-N. Chen, J.-J. Wang, and L.-Q. Chen, "Ferroelectric domain structures and temperature-misfit strain phase diagrams of $K_{1-x}Na_xNbO_3$ thin films: A phase-field study," Appl. Phys. Lett. **115**, 092902 (2019).

[25] L. Bogula, L. von Helden, C. Richter, M. Hanke, J. Schwarzkopf, and M. Schmidbauer, "Ferroelectric phase transitions in multi-domain $K_{0.9}Na_{0.1}NbO_3$ strained thin films," Nano Futures **4**, 035005 (2020).

[26] M. Schmidbauer, D. Braun, T. Markurt, M. Hanke, and J. Schwarzkopf, "Strain engineering of monoclinic domains in $K_{0.9}Na_{0.1}NbO_3$ epitaxial layers: A pathway to enhanced piezoelectric properties," Nanotechnology **28**, 24LT02 (2017).

[27] L.-Q. Chen, "Phase-field method of phase transitions/domain structures in ferroelectric thin films: A review," J. Am. Ceram. Soc. **91**, 1835–1844 (2008).

[28] J.-J. Wang, B. Wang, and L.-Q. Chen, "Understanding, predicting, and designing ferroelectric domain structures and switching guided by the phase-field method," Annu. Rev. Mater. Res. **49**, 127–152 (2019).

[29] Y. L. Li, S. Y. Hu, Z. K. Liu, and L. Q. Chen, "Effect of electrical boundary conditions on ferroelectric domain structures in thin films," Appl. Phys. Lett. **81**, 427–429 (2002).

[30] Y. L. Li, S. Y. Hu, Z. K. Liu, and L. Q. Chen, "Effect of substrate constraint on the stability and evolution of ferroelectric domain structures in thin films," Acta Mater. **50**, 395–411 (2002).

[31] L. Liang, Y. L. Li, L.-Q. Chen, Y. Hu, and G.-H. Lu, "A thermodynamic free energy function for potassium niobate," Appl. Phys. Lett. **94**, 072904 (2009).

[32] H. Pohlmann, J.-J. Wang, B. Wang, and L.-Q. Chen, "A thermodynamic potential and the temperature-composition phase diagram for single-crystalline $K_{1-x}Na_x$ NbO_3 ($0\leq x\leq 0.5$)," Appl. Phys. Lett. **110**, 102906 (2017).

[33] B. Wang, L. Bogula, A. Ladera, J.-J. Wang, and L.-Q. Chen, "Phase stability and three-dimensional structures of polydomains in orthorhombic ferroelectric thin films under anisotropic misfit strains," (unpublished).

[34] C. Hirschle, J. Schreuer, S. Ganschow, and L. Peters, "Thermoelastic anisotropy in $NdScO_3$ and $NdGaO_3$ perovskites," Mater. Chem. Phys. **254**, 123528 (2020).

[35] H. D. Megaw, "The thermal expansion of interatomic bonds, illustrated by experimental evidence from certain niobates," Acta Crystallogr. A **24**, 589–604 (1968).

[36] I. T. Weber, A. Rousseau, M. Guilloux-Viry, V. Bouquet, and A. Perrin, "Microstructure comparison between $KNbO_3$ thin films grown by polymeric precursors and PLD methods," Solid State Sci. **7**, 1317–1323 (2005).

[37] J. Sellmann, J. Schwarzkopf, A. Kwasniewski, M. Schmidbauer, D. Braun, and A. Duk, "Strained ferroelectric $NaNbO_3$ thin films: Impact of pulsed laser deposition growth conditions on structural properties," Thin Solid Films **570**, 107–113 (2014).

[38] T.-H. Lee, D.-H. Kim, B.-Y. Kim, H.-Y. Choi, J.-H. Oh, C.-Y. Kang, and S. Nahm, "Structural and electrical properties of $KNbO_3$ thin film grown on a Pt/Ti/SiO_2/Si substrate using the RF magnetron sputtering method," Acta Mater. **112**, 53–58 (2016).

[39] J. Schwarzkopf, M. Schmidbauer, T. Remmele, A. Duk, A. Kwasniewski, S. Bin Anooz, A. Devi, and R. Fornari, "Strain induced phase transitions in $NaNbO_3$ epitaxial thin films grown by metal-organic chemical vapor deposition," J. Appl. Crystallogr. **45**, 1015–1023 (2012).

[40] J. Als-Nielsen and D. McMorrow, *Elements of Modern X-ray Physics* (Wiley, 2011).

[41] A. S. Disa, F. J. Walker, and C. H. Ahn, "High-resolution crystal truncation rod scattering: Application to ultrathin layers and buried interfaces," Adv. Mater. Interfaces **7**, 1901772 (2020).

[42] M. Schmidbauer, P. Schäfer, S. Besedin, D. Grigoriev, R. Köhler, and M. Hanke, "A novel multi-detection technique for 3D reciprocal space mapping in grazing incidence x-ray diffraction," J. Synchrotron Radiat. **15**, 549–557 (2008).

[43] Z. L. Luo, H. Huang, H. Zhou, Z. H. Chen, Y. Yang, L. Wu, C. Zhu, H. Wang, M. Yang, S. Hu, H. Wen, X. Zhang, Z. Zhang, L. Chen, D. D. Fong, and C. Gao, "Probing the domain structure of $BiFeO_3$ epitaxial films with three-dimensional reciprocal space mapping," Appl. Phys. Lett. **104**, 182901 (2014).

[44] D. Braun, M. Schmidbauer, M. Hanke, and J. Schwarzkopf, "Hierarchy and scaling behaviour of multi-rank domain patterns in ferroelectric $K_{0.9}Na_{0.1}NbO_3$ strained films," Nanotechnology **29**, 015701 (2018).

[45] See https://www.anton-paar.com for detailed technical specifications.

[46] R. Xu, S. Liu, I. Grinberg, J. Karthik, A. R. Damodaran, A. M. Rappe, and L. W. Martin, "Ferroelectric polarization reversal via successive ferroelastic transitions," Nat. Mater. **14**, 79–86 (2015).

[47] W. L. Li, T. D. Zhang, Y. F. Hou, Y. Zhao, D. Xu, W. P. Cao, and W. D. Fei, "Giant piezoelectric properties of BZT–0.5BCT thin films induced by nanodomain structure," RSC Adv. **4**, 56933 (2014).